

Deformation and chaining of flexible shells in a nematic solvent

Andrew DeBenedictis and Timothy J. Atherton*
*Department of Physics and Astronomy, Tufts University,
574 Boston Avenue, Medford, Massachusetts 02155, USA*

Andrea L. Rodarte and Linda S. Hirst
*Department of Physics, University of California, Merced,
5200 Lake Road, Merced, California 95343, USA*

A micrometer-scale elastic shell immersed in a nematic liquid crystal may be deformed by the host if the cost of deformation is comparable to the cost of elastic deformation of the nematic. Moreover, such inclusions interact and form chains due to quadrupolar distortions induced in the host. A continuum theory model using finite elements is developed for this system, using mesh regularization and dynamic refinement to ensure quality of the numerical representation even for large deformations. From this model, we determine the influence of the shell elasticity, nematic elasticity and anchoring condition on the shape of the shell and hence extract parameter values from an experimental realization. Extending the model to multi-body interactions, we predict the alignment angle of the chain with respect to the host nematic as a function of aspect ratio, which is found to be in excellent agreement with experiments and greatly improves upon previous theoretical predictions.

I. INTRODUCTION

An important application of nematic liquid crystals (LCs) is as guides for the self assembly of included colloidal particles [1–4]. Chemical treatment of the particles may induce a locally preferred orientation of the adjacent nematic on their surface and induce elastic distortions in the bulk liquid crystal. Elasticity-mediated interactions between particles cause micron-sized particles to self-organize into chains or clusters that are strongly ($\sim 1000k_B T$) bound together [2, 5–7]. Much smaller nanoparticles (NPs) disperse uniformly in the isotropic phase but can be sculpted into a variety of structures including networks and shells by kinetic effects as the host undergoes a transition into a liquid crystalline phase [1, 8, 9]. Self-assembly of nanoparticles in LCs can therefore exploit nucleation and growth as would occur in an isotropic fluid [10, 11], but the liquid crystalline order permits additional control over the self-assembled structure [9].

Hierarchical structures can be formed by combining these mechanisms. Two co-authors of this paper (Rodarte, Hirst) created nanoparticle shells [12] by cooling a solution of mesogen-functionalized quantum dots in 5CB from the isotropic to nematic phase. The nanoparticles are driven to the boundary of the vanishing isotropic phase and by a nucleating inner nematic domain; they aggregate and solidify, leaving behind a shell. As shown in Fig. 1 shells then migrate after their formation to align in long chains due to the elastic interactions and, remarkably, adopt a more elongated morphology over time.

In this paper, we develop a model of the elongation and chaining process by minimizing the elastic free en-

ergy with both with respect to the spatially varying orientation of the liquid crystal *and* the shape of the shell. We predict the shape as a function of the elastic constants for both the nematic and the shell, and determine the orientation of the chains with respect to the bulk nematic. Results are compared with experiment and earlier models that neglect the shape of the particles [6, 13].

Shape-order optimization problems such as the shells in this paper are challenging because few analytical results are available and computational approaches must maintain the quality of the numerical representation during the optimization. A related and widely studied problem of similar character is to determine the shape of a *tactoid*, a droplet of nematic liquid crystal in a host solvent. While a rich variety of tactoid shapes is observed in lyotropic systems [14–16], including some that are not simply-connected [17, 18], thermotropic liquid crystals such as 5CB generally form spherical droplets because of the surface tension between the LC and host tends to be much larger than the cost of elastic deformations. For the shells in [12] and considered here, significant deformation occurs because the surface in question is not the interface between the LC and a host fluid but rather the surface of the solid shell that is surrounded inside and out by the LC.

Because no theoretical technique can simultaneously resolve the molecular scale order of the liquid crystal and the micron-sized shape of the tactoid, theoretical work requires a trade off between size and resolution. Prior work includes Monte Carlo methods predict elongation of thermotropic LCs [19], Molecular Dynamics simulations that show elongation and spontaneous chiral order in nanoscale droplets [20–23] and continuum theory [24, 25] that nonetheless assumes a rigid idealized shape for the tactoid boundary.

Recently [26], we created a finite element continuum theory model to determine tactoid shape incorporating a

* timothy.atherton@tufts.edu

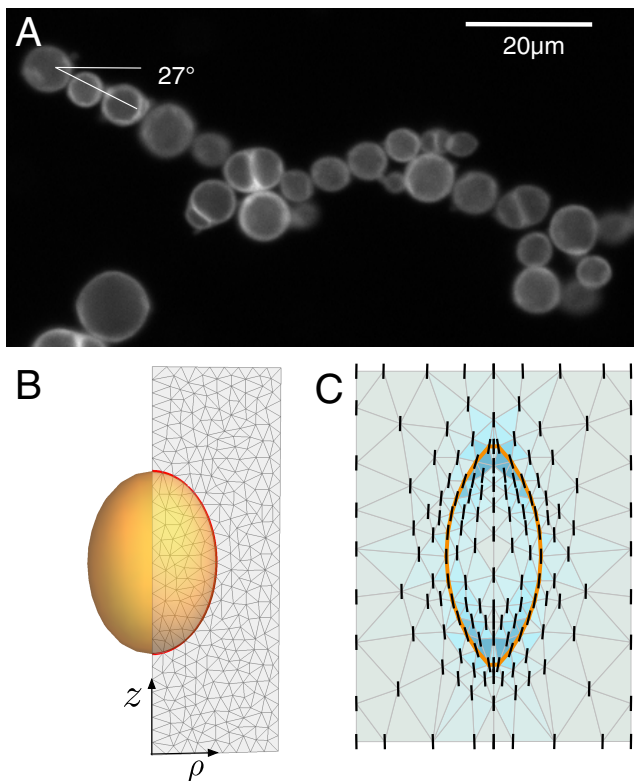


Figure 1. (Color online) **A** Fluorescence microscopy images of quantum dot microspheres[12] show subtly elongated shells that form chains, here at 27° to the alignment axis of the nematic host. **B** Schematic of the computational domain. **C** Fully relaxed simulation with $\Gamma_\sigma = 10$, $\Gamma_\kappa = 0$, and $\Gamma_W = 10$, shaded to indicate the relative energy of each mesh face. Two copies of the computational domain are depicted, one reflected about the z axis, to assist visualization.

new dynamic mesh control algorithm that ensures the numerical scheme remains accurate and stable during shape minimization. Here we will adapt the same strategy to model the shells discussed above. The paper is structured as follows: in Section II the model is described. In section III A the results are compared to experimental observations. The chaining phenomenon is studied in section III B using an extension of the model described in section II. Finally, conclusions and future work are presented in Section IV.

II. MODEL

The system comprises a nanoparticle shell with nematic liquid crystal on both the interior and exterior. The total free energy comprises three contributions,

$$F = F_s + F_n + F_a, \quad (1)$$

i.e. the elastic energy of deforming the shell, the elastic energy of the nematic and an anchoring term that couples the nematic to the shell. The shells are composed

of nanoparticles stabilized by ligand-ligand interactions with a very short range attractive attraction[12]. These interactions therefore resist changes in the area of the shell. Since the shells are only a few nanoparticles thick, we *a priori* expect the bending energy to be negligible, but nonetheless include it in the energy to determine its effect on the shape. The shell elastic contribution to (1) is therefore,

$$F_s = \sigma \int_{\partial S} dA + \kappa \int_{\partial S} (H - H_0)^2 dA$$

where σ is the surface tension, H is the mean curvature and H_0 is a prescribed mean curvature. Because the shells first form at the interface of an approximately spherical isotropic region at a critical radius R , we assume the preferred mean curvature H_0 is that of the initial sphere ($1/R$). In practice, we find that H_0 and κ have covariant effects on the final shape, so this choice is somewhat arbitrary.

The elastic energy of the LC is the Frank energy[27],

$$F_n = \int_{S,S'} dV \left[K_1 (\nabla \cdot \mathbf{n})^2 + K_2 (\mathbf{n} \cdot \nabla \times \mathbf{n})^2 + K_3 |\mathbf{n} \times \nabla \times \mathbf{n}|^2 \right], \quad (2)$$

where K_1 , K_2 , and K_3 are the splay, twist, and bend elastic constants and the integral is taken over the entire simulation volume, i.e. both the interior S and exterior S' of the shell. A local constraint $\mathbf{n} \cdot \mathbf{n} = 1$ is enforced to ensure the director remains a unit vector.

Finally, the anchoring term,

$$F_a = W \int_{\partial S} \|\mathbf{n} - \mathbf{n}_e\|^2 dA, \quad (3)$$

imposes a preferred orientation \mathbf{n}_e relative to the shell normal with associated energy W . Because the shells are ligand-stabilized, we additionally impose a volume constraint,

$$\int_S dV = V_0. \quad (4)$$

We non-dimensionalize the problem in the usual way using Λ , a length scale of the order of the size of the shell, by changing variables $x \rightarrow \Lambda x'$ and dividing through by $K_1 \Lambda$. Hence, the energy (1) becomes,

$$\begin{aligned} \frac{F}{K_1 \Lambda} &= \Gamma_\sigma \int_{\partial S} dA + \Gamma_\kappa \int_{\partial S} (H' - H'_0)^2 dA \\ &+ F_n / K_1 + \Gamma_W \int_{\partial S} \|\mathbf{n} - \mathbf{n}_e\|^2 dA. \end{aligned} \quad (5)$$

Hence we introduce dimensionless parameters $\Gamma_\sigma = \frac{\sigma \Lambda}{K_1}$, $\Gamma_\kappa = \frac{\kappa}{K_1 \Lambda^3}$, and $\Gamma_W = \frac{W \Lambda}{K_1}$, that represent the relative strengths of the surface tension, mean squared curvature, and anchoring energy relative to the elastic energy.

The functional (5) is discretized as follows. First, we exploit the apparent cylindrical symmetry of the shells

to work in cylindrical polar coordinates (ρ, ϕ, z) . The computational domain, shown in Fig. 1B, is the (ρ, z) plane that must be swept out in ϕ to recover the full 3D solution and is discretized into triangular elements. The initially spherical shell surface is specified as a sequence of edges terminating at top and bottom on the $\rho = 0$ line. The mean curvature H of the shell at a given vertex on the shell is calculated using the discrete method from [28]. Director values are stored on each vertex and parametrized in cylindrical coordinates, $\mathbf{n} = (n_\rho, n_\phi, n_z)$ with appropriate derivatives in (2) re-expressed in these coordinates. Interpolation of the director between vertices is performed using a special spherical weighted average [29] that maintains unit length at all points. The Frank energy of each element is then computed by gaussian quadrature [30]. The anchoring energy (3) is also computed along the shell by gaussian quadrature.

Having constructed a finite element approximation to (5), we minimize it using gradient descent with respect to both the director values and vertex positions from an initial state with $\mathbf{n} = n_z$ at all vertices. To maintain a well-behaved mesh, we supplement the target functional with auxiliary functionals as described in [26] that promote equiangular elements and uniform energy density between adjacent elements. Additionally, local refinement and coarsening is performed to capture adequate detail in regions of high energy density. Fig. 1C shows a converged solution in which the local refinement and energy density reveal the bipolar field adopted by the nematic. The system is considered to have converged when the timestep-normalized percent change to the energy is less than 10^{-6} over two cycles of steps to relax both the vertex location and director orientation. We explicitly test all solutions for stability by computing the bordered Hessian matrix G and testing that the number of constraints plus the number of degrees of freedom for the system is larger than the negative index of inertia plus the corank of G .

III. RESULTS

A. Shell shape

We ran a series of simulations varying the coefficients Γ_σ , Γ_κ and Γ_W to determine how the final shape of the shell depends on these parameters and hence identify the space of shell shapes accessible by this mechanism. One measure of the final shape is the aspect ratio a , which is displayed in Fig. 2 as a function of the surface tension. The high aspect ratios obtained indicate that the mesh regularization procedure described is effective in permitting large physical deviations from the initial shape. The simulations reproduce aspect ratios similar to those observed experimentally ($0.9 \leq a \leq 1.3$) under two distinct conditions: first, systems where the mean squared curvature term dominates; second, systems dominated by surface tension. Either of these cases suggests, as we expect,

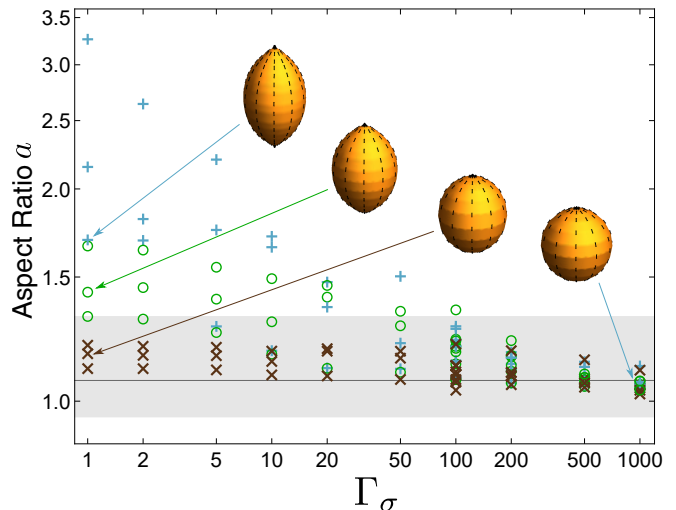


Figure 2. Aspect ratio for simulated shells as a function of surface tension. Cyan crosses, green circles, and brown exes denote respectively simulations with $\Gamma_\kappa = 0$, $\Gamma_\kappa = 0.1$, and $\Gamma_\kappa = 1.0$. Variation of aspect ratio within a set of points with the same Γ_σ and Γ_κ is caused by variation in Γ_W , typically with higher aspect ratios corresponding to stronger anchoring. Insets visualize the shells for selected points, all of which have $\Gamma_W = 100$. The gray region denotes the range of aspect ratios observed in the experimental data, with the darker line indicating the median of 1.07.

that the interactions between ligands of the nanoparticles are considerably stronger than interactions between LC molecules. Indeed, the experimental shells remain stable even when the surrounding nematic phase is heated to isotropic above 34°C and remain stable up to about 100°C .

Looking in more detail at the predicted shape of the shells displayed in the insets of fig. 2 there are two distinct morphologies: Surface tension dominated shells form a characteristic cusp at the poles; conversely mean squared curvature dominated shells instead favor smooth poles. The fluorescence microscopy image shown in fig. 1A shows evidence of cusps, and so we conclude that the shell elasticity is dominated by surface tension. This is expected a classic result from shell elasticity: the ratio of bend energy to stretching energy is of order $(R/h)^2$ where R is the shell radius and h is the shell thickness [31]. We estimate the shell thickness to be 10 to 100 times smaller than the radius, which suggests that $\Gamma_\sigma/\Gamma_\kappa$ lies between 100 to 10,000.

Fig. 2 therefore allows us to predict the shapes that would result from changing the experimental system. For example, use of a LC with larger elastic constants would decrease Γ_σ , resulting in more elongated shells. Similarly, decreasing (increasing) the concentration of nanoparticles in the initial system would result in smaller (larger) shells [12], which have a smaller (larger) Γ_σ and thus will elongate more (less).

We now turn to the configuration of the liquid crystal

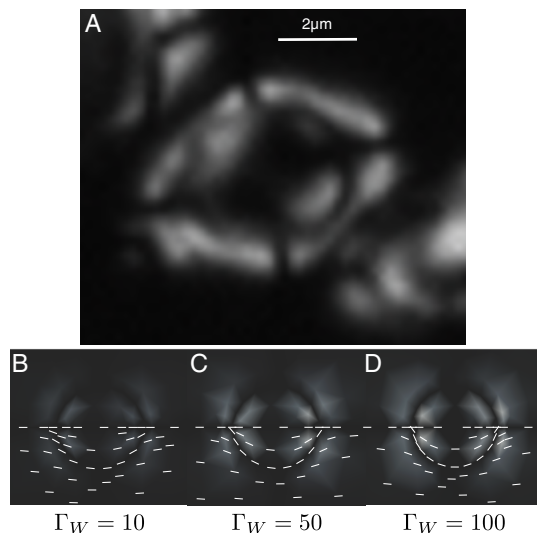


Figure 3. **A** An experimental crossed-polarizer image of a shell imaged close to the central plane. **B-D** Simulated crossed-polarizer images for three shells with different anchoring strengths ($\Gamma_W = 10, 50,$ and 100) and aspect ratios equal to the median aspect ratio observed experimentally. The director field superimposed over the simulated images shows stronger anchoring conditions leading to more curvature in the nematic field.

around and inside the shell. To facilitate a comparison with experiment, an approximate crossed-polarizer microscope image is generated from each configuration. A very simple optical model is used, treating the LC as a single anisotropic layer in the $y = 0$ plane between two crossed-polarizers above and below the LC. Thus, the intensity I at a given point is

$$I = \cos^2 \phi \sin^2 \phi, \quad (6)$$

where ϕ is the angle of the director off of the z axis. We emphasize that this is quite a crude approximation of a true crossed-polarizer image, using only the 2D slice of the director field. Moreover, the optical properties of the NP shell itself are unknown, however motivated by the experimental images, we assume that no light passes through the pixels that lie directly on the shell boundary at $y = 0$.

Results are displayed in panels B through D of Fig. 3 that show simulated microscope images with different anchoring strengths but aspect ratios all within 2% of the median experimental aspect ratio. In spite of the very simple optical model, the simulated images reproduce the main features of the experimental image shown in 3A: they possess a dark band along the axis of symmetry, indicating LC alignment along the axis. The dark band perpendicular to this axis denotes a region of LC alignment parallel to the vertical polarizer. Bright regions appear inside and outside of the shell where the director field distorts to match both the anchoring condition at the shell and either the axis of symmetry or the

far-field director orientation. Weak anchoring requires less perfect matching of the easy axis at the shell, and thus less LC field deformation and dimmer images. The similarity between the two strongest anchoring cases and the experimental image suggests anchoring strength of at least $\Gamma_W = 50$. This corresponds to a value of W of order 10^{-5} J/m^2 , consistent with characterizations of strong anchoring [32, 33]. That cases with strong anchoring require $\Gamma_\sigma \geq 500$ to achieve aspect ratios of 1.07 is consistent with the surface tension-dominated system.

B. Shell-shell interactions and chaining

After formation, the NP shells are observed to migrate over the course of minutes to form chains aligned at some angle to the host nematic (Fig. 1A). Previous studies with colloidal glass spheres instead of shells behave similarly, as this feature is generic to particles that produce a quadrupolar distortion field in the host nematic [2, 33, 34]. These authors report observed alignment angles of $\sim 30^\circ$ for particles with parallel anchoring, while our NP shells align at angles between 25° and 35° (Fig. 1A). Recently, chaining has also been observed in ferromagnetic nanoparticles[35], although the chaining angles observed there are somewhat higher $\sim 54^\circ$ which is likely because of the presence of shell-shell interactions other than elasticity.

Prior theoretical calculations predict much larger chaining angles, between 45° and 49° , than those observed either with shells or microspheres. This is because they take a far-field approximation and neglect short-range distortions induced by the particle shape [6, 13, 36, 37]. Here, we will adapt the shape evolution technique developed above to include two shells that are mobile and hence able to locate an equilibrium state. Because the shells composing these chains do not share axes of symmetry, the cylindrical domain above cannot be used. Instead, we develop a two-dimensional model that includes only the projections of the shells onto the $y = 0$ plane.

Minimization of elastic deformations in the host nematic drives the alignment of the shells. However, from the results in section III A these elastic forces are weak compared to the surface tension and anchoring forces that define the shapes of the shells and the LC orientation at the shell-nematic interfaces. The shape of the shells and anchoring conditions are therefore fixed and so the only the elasticity term of (1) is minimized with respect to the shape of the host nematic domain.

To initialize the simulation, shell shapes and LC director fields at the LC-shell interface are taken from final states of the simulations described in section III A to use in the chaining model. For each run, a mesh is built containing two such shells with their axes of symmetry along the z axis, but offset such that their centers form an angle θ_0 with this axis. Again, we take gradient descent steps alternately to relax the vertex locations, director

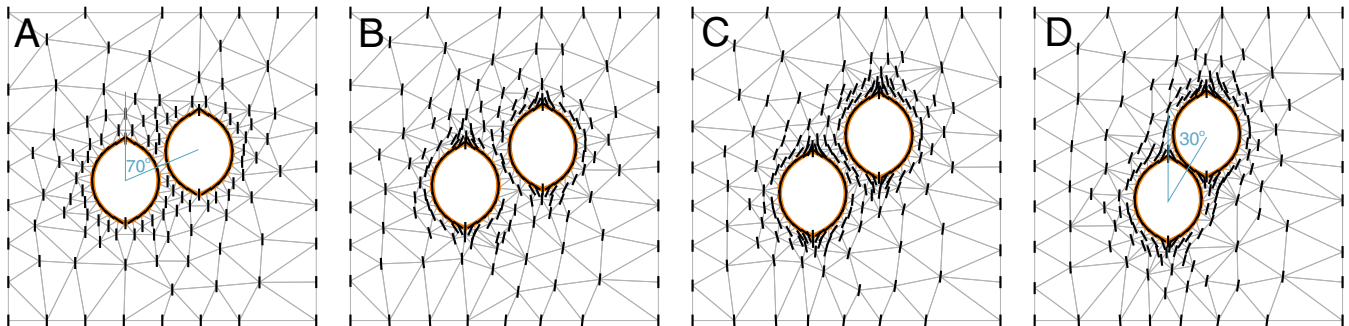


Figure 4. **A-D** Simulation snapshots of two shells with aspect ratio = 1.18 relaxing from $\theta_0 = 70^\circ$ to $\theta_p = 30^\circ$. The shells repel initially, before finding their preferred alignment angle and attracting one another.

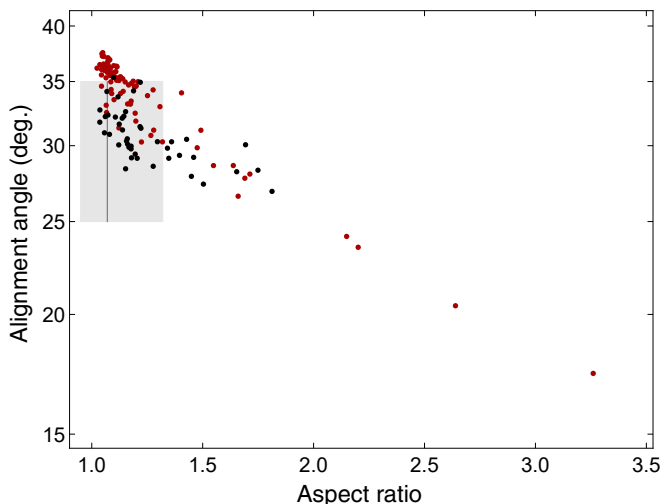


Figure 5. (Color online) Preferred alignment angle θ_p as a function of shell aspect ratio for all of the simulated cases shown in fig. 2. The black series contains cases with strong anchoring ($\Gamma_W > 50$) while the red series contains cases with weaker anchoring ($\Gamma_W \leq 50$). The gray region denotes the range of aspect ratios and angles observed in the experimental data, with the darker line indicating the median of 1.07.

orientations, and mesh quality. As the anchoring of the LC to the shell boundary is fixed, the interior regions of the shells does not contribute to the alignment and is not included in the computational domain. The preferred alignment angle θ_p does not depend on θ_0 .

Results from a typical run are shown in Fig. 4. Panels A through D show selected snapshots from a simulation where the starting alignment angle $\theta_0 = 70^\circ$. Initially, the shells repel each other, before rotating around to find a preferable angle. Once at this angle, the space between the shells collapses as nematic forces attract them. This behavior of repulsion at angles close to 0° or 90° and attraction at intermediate angles is well-documented experimentally [33, 34].

Fig. 5 displays the calculated chaining angle as a function of the aspect ratio of the NP shells with strong (black) and weak (red) anchoring. As aspect ratio in-

creases, the chaining angle is reduced. Noise in the plot is due to variations in the anchoring condition and bend modulus from the initial configuration. For shells with aspect ratios in the range observed experimentally, we see preferred angles mostly from 28° to 36° , which is in very good agreement with the chains seen experimentally. Furthermore, extrapolation of the strong anchoring data in the limit of $a \rightarrow 1$, i.e. spherical colloidal particles with rigid anchoring, $\theta_p = 32$, which agrees very well with the 30° reported by other authors than any previous method.

IV. CONCLUSION

We present a continuum theory finite element model for deformation and two body interactions of a flexible shell in a nematic liquid crystal. The model features dynamic mesh remodeling utilizing auxiliary functionals to maintain accuracy despite large deformations from the initial configuration. The model is used to simulate experimentally observed elongation and chaining of mesogen-functionalized nanoparticle shells that form as the LC is quenched into the nematic phase. Because the elastic behavior of these shells is unknown, the model enables us to extract the relative contribution of shell elasticity, nematic elasticity and anchoring from the observed shapes. By comparing simulations with experimental images, we determine surface tension and anchoring dominate the shell shape.

Extending the model to incorporate multiple shells, we predict the chaining angles attained by the shells, and determine the dependence of the chaining angles on the aspect ratios of the shells. Furthermore, our model predicts the chaining angle of spherical particles with strong planar anchoring in a nematic LC far more accurately than any previous theoretical treatment.

Our simulations cover a wide range of parameter space, so information from these results enables us to design systems with particular shell sizes, shapes, and alignment angles. This ability to control and tune particle shape by an highly scalable self-assembly method is valuable as part of designing hierarchical processes. Furthermore, the simulation methodology presented is computation-

ally cheap and readily adapted, with little modification, to a wide variety of shape-order problems involving soft materials.

ACKNOWLEDGMENTS

ADB is supported by a Tufts University Burlingame Fellowship. TJA acknowledges support from the National

Science Foundation under grant no. DMR-1654283. TJA is also supported by a Cottrell Award from the Research Corporation for Science Advancement. LSH and ALR acknowledge financial support from the National Science Foundation grant no. DMR-CBET-1507551. This work was partly performed at the Aspen Center for Physics, which is supported by National Science Foundation grant PHY-1066293.

-
- [1] S. P. Meeker, W. C. K. Poon, J. Crain, and E. M. Terentjev, *Phys. Rev. E* **61**, R6083 (2000).
- [2] I. Mušević, M. Škarabot, U. Tkalec, M. Ravnik, and S. Žumer, *Science* **313**, 954 (2006).
- [3] I.-H. Lin, G. M. Koenig, J. J. de Pablo, and N. L. Abbott, *The Journal of Physical Chemistry B* **112**, 16552 (2008), pMID: 19049270.
- [4] G. M. Koenig, I.-H. Lin, and N. L. Abbott, *Proceedings of the National Academy of Sciences* **107**, 3998 (2010).
- [5] P. Poulin, H. Stark, T. C. Lubensky, and D. A. Weitz, *Science* **275**, 1770 (1997).
- [6] P. Poulin and D. A. Weitz, *Phys. Rev. E* **57**, 626 (1998).
- [7] M. Škarabot, M. Ravnik, S. Žumer, U. Tkalec, I. Poberaj, D. Babič, N. Osterman, and I. Mušević, *Phys. Rev. E* **77**, 031705 (2008).
- [8] J. Milette, S. J. Cowling, V. Toader, C. Lavigne, I. M. Saez, R. Bruce Lennox, J. W. Goodby, and L. Reven, *Soft Matter* **8**, 173 (2012).
- [9] A. L. Rodarte, R. J. Pandolfi, S. Ghosh, and L. S. Hirst, *J. Mater. Chem. C* **1**, 5527 (2013).
- [10] J. B. Miller, A. C. P. Usselman, R. J. Anthony, U. R. Kortshagen, A. J. Wagner, A. R. Denton, and E. K. Hobbie, *Soft Matter* **10**, 1665 (2014).
- [11] H. Wu, L. X. Chen, X. Q. Zeng, T. H. Ren, and W. H. Briscoe, *Soft Matter* **10**, 5243 (2014).
- [12] A. L. Rodarte, B. H. Cao, H. Panesar, R. J. Pandolfi, M. Quint, L. Edwards, S. Ghosh, J. E. Hein, and L. S. Hirst, *Soft Matter* **11**, 1701 (2015).
- [13] H. Stark, *Physics Reports* **351**, 387 (2001).
- [14] V. H. Zocher, *Zeitschrift für Anorg. und Allg. Chemie* **147**, 91 (1925).
- [15] V. H. Zocher and K. Jacobsohn, *Kolloid Beih.* **28**, 167 (1929).
- [16] J. D. Bernal and I. Fankuchen, *J. Gen. Physiol.* **25**, 111 (1941).
- [17] C. Casagrande, P. Fabre, M. A. Guedeau, and M. Veyssie, *Europhys. Lett.* **3**, 73 (1987).
- [18] Y.-K. Kim, S. V. Shiyakovskii, and O. D. Lavrentovich, *J. Phys. Condens. Matter* **25**, 404202 (2013).
- [19] M. A. Bates, *Chem. Phys. Lett.* **368**, 87 (2003).
- [20] M. Tsige, M. P. Mahajan, C. Rosenblatt, and P. L. Taylor, *Phys. Rev. E* **60**, 638 (1999).
- [21] R. Berardi, A. Costantini, L. Muccioli, S. Orlandi, and C. Zannoni, *The Journal of Chemical Physics* **126**, 044905 (2007).
- [22] L. F. Rull, J. M. Romero-Enrique, and A. Fernandez-Nieves, *The Journal of Chemical Physics* **137**, 034505 (2012).
- [23] D. Vanzo, M. Ricci, R. Berardi, and C. Zannoni, *Soft Matter* **8**, 11790 (2012).
- [24] A. V. Kaznacheev, M. M. Bogdanov, and S. A. Taraskin, *J. Exp. Theor. Phys.* **95**, 57 (2002).
- [25] P. Prinsen and P. Van Der Schoot, *Eur. Phys. J. E* **13**, 35 (2004).
- [26] A. DeBenedictis and T. J. Atherton, *Liquid Crystals* **43**, 2352 (2016).
- [27] F. C. Frank, *Discuss. Faraday Soc.* **25**, 19 (1958).
- [28] N. Dyn, K. Hormann, S.-J. Kim, and D. Levin (Vanderbilt University, Nashville, TN, USA, 2001) Chap. Optimizing 3D Triangulations Using Discrete Curvature Analysis, pp. 135–146.
- [29] S. R. Buss and J. P. Fillmore, *ACM Transactions on Graphics (TOG)* **20**, 95 (2001).
- [30] D. A. Dunavant, *International Journal for Numerical Methods in Engineering* **21**, 1129 (1985).
- [31] L. D. Landau, L. P. Pitaevskii, A. M. Kosevich, and E. M. Lifshitz, “Theory of elasticity,” (2012).
- [32] O. V. Kuksenok, R. W. Ruhwandl, S. V. Shiyakovskii, and E. M. Terentjev, *Phys. Rev. E* **54**, 5198 (1996).
- [33] R. W. Ruhwandl and E. M. Terentjev, *Phys. Rev. E* **55**, 2958 (1997).
- [34] I. I. Smalyukh, O. D. Lavrentovich, A. N. Kuzmin, A. V. Kachynski, and P. N. Prasad, *Phys. Rev. Lett.* **95**, 157801 (2005).
- [35] I. Dierking, M. Heberle, M. Osipov, and F. Giesselmann, *Soft Matter* (2017).
- [36] S. Ramaswamy, R. Nityananda, V. A. Raghunathan, and J. Prost, *Molecular Crystals and Liquid Crystals Science and Technology. Section A. Molecular Crystals and Liquid Crystals* **288**, 175 (1996).
- [37] T. Araki and H. Tanaka, *Phys. Rev. Lett.* **97**, 127801 (2006).